CHAOS-2—a geomagnetic field model derived from one decade of continuous satellite data

Nils Olsen,[1]* Mioara Mandea,[2] Terence J. Sabaka[3] and Lars Tøffner-Clausen[1]

[1]*DTU Space, Juliane Maries Vej 30, 2100 Copenhagen, Denmark. E-mail: nio@space.dtu.dk*
[2]*Helmholtz-Zentrum Potsdam, Deutsches GeoForschungsZentrum, 14473 Potsdam, Germany*
[3]*Geodynamics Branch, NASA GSFC, Greenbelt, MD, USA*

SUMMARY

We have derived a model of the near-Earth's magnetic field using more than 10 yr of high-precision geomagnetic measurements from the three satellites Ørsted, CHAMP and SAC-C. This model is an update of the two previous models, CHAOS (Olsen *et al.* 2006) and xCHAOS (Olsen & Mandea 2008). Data selection and model parameterization follow closely those chosen for deriving these models. The main difference concerns the maximum spherical harmonic degree of the static field ($n = 60$ compared to $n = 50$ for CHAOS and xCHAOS), and of the core field time changes, for which spherical harmonic expansion coefficients up to $n = 20$ are described by order 5 splines (with 6-month knot spacing) spanning the years from 1997.0 to 2009.5.

Compared to its predecessors, the temporal regularization of the CHAOS-2 model is also modified. Indeed, second and higher order time derivatives of the core field are damped by minimizing the second time derivative of the squared magnetic field intensity at the core–mantle boundary. The CHAOS-2 model describes rapid time changes, as monitored by the ground magnetic observatories, much better than its predecessors.

Key words: ???

1 INTRODUCTION

The launch of the Ørsted satellite in 1999 February marked the beginning of the 'International Decade of Geopotential Research'. Ørsted was followed by the CHAMP satellite and the SAC-C satellite, launched in 2000 July and November, respectively. All three missions carry essentially the same instrumentation and provide high-quality and high-resolution magnetic field observations from space. The three satellites sense the various internal and external field contributions differently, due to their different altitudes (Ørsted: 630–860 km, CHAMP: 310–450 km; SAC-C: 700 km) and drift rates through local time.

Various magnetic field models of increasing complexity have been derived using data from these satellites, from 'snapshot models' that describe the field at a specific epoch (Olsen *et al.* 2000a,b) over models for which the time dependence of the core field is parameterized by a Taylor expansion in time (Olsen 2002; Langlais *et al.* 2003; Maus *et al.* 2005, 2006; Thomson & Lesur 2007) to models with spline-representation of the time dependence (Olsen *et al.* 2006; Lesur *et al.* 2008; Olsen & Mandea 2008). The present

paper describes an updated version of the CHAOS geomagnetic field model of Olsen *et al.* (2006), denoted as CHAOS-2 (see Olsen & Mandea (2008) for a description of xCHAOS, a predecessor of CHAOS-2).

The goal of CHAOS-2 is to provide a good representation of the core field changes by making use of 10 yr of continuous high-precision satellite magnetic observations. In particular, the model aims at describing core field changes with high spatial resolution of the first time derivative (linear secular variation), and high temporal resolution (rapid field changes). We have derived two model versions: CHAOS-2s is more heavily regularized in time and therefore smoother, while CHAOS-2r is less heavily regularized and thus rougher. In following we use the more generic name CHAOS-2 to describe features which are common to both model versions.

2 DATA SELECTION AND MODEL PARAMETERIZATION

We use Ørsted scalar and vector data between 1999 March and 2009 March (vector data only until 2005 December), CHAMP vector and scalar data between 2000 August and 2009 March (vector data only after 2001 January), and SAC-C scalar data between 2001 January and 2004 December. These satellite data are selected using

*Also at: Niels Bohr Institute of Copenhagen University, Juliane Maries Vej 30, 2100 Copenhagen, Denmark.
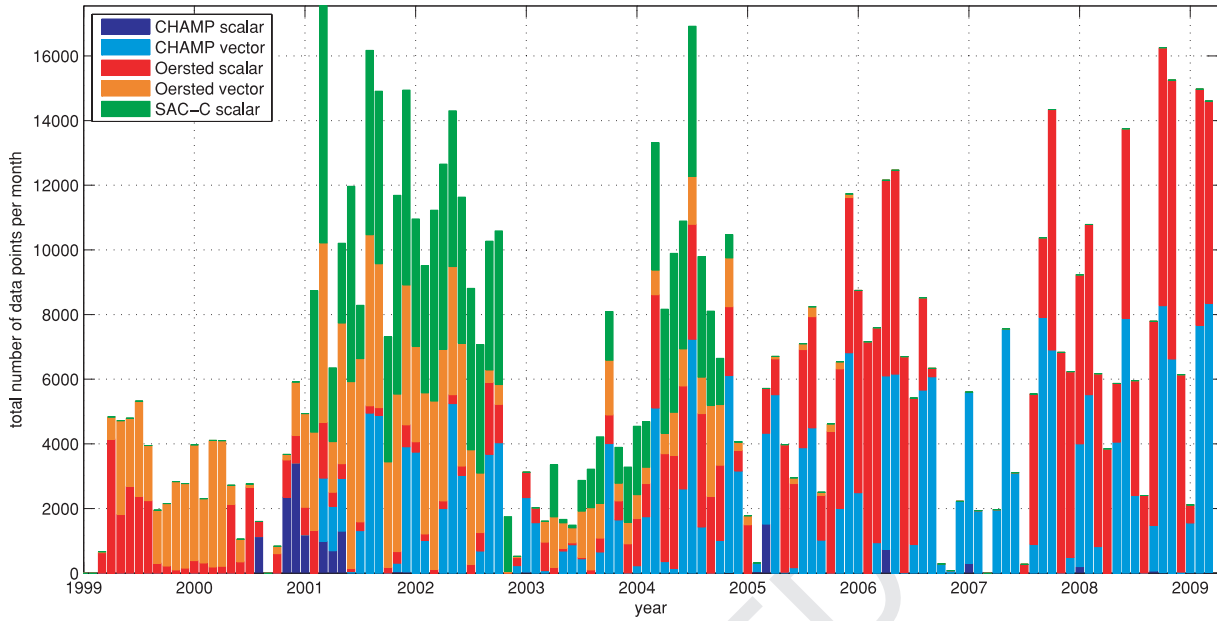
Figure 1. Total number of non-polar magnetic field observations (stacked histogram) as a function of time.

the same criteria as for the CHAOS model (Olsen *et al.* 2006): (1) at all latitudes we require that the D_{st}-index measuring the strength of the magnetospheric ring-current does not change by more than 2 nT hr^{-1}; (2) at non-polar latitudes (equatorward of $\pm 60^{\circ}$ dipole latitude) we require for the geomagnetic activity index $Kp \leq 2^{o}$; (3) for regions poleward of 60° dipole latitude the merging electric field at the magnetopause has to be less than 0.8 mV m^{-1}; (4) only data from dark regions (sun 10° below horizon) are used; (5) vector data are taken for dipole latitudes equatorward of $\pm 60^{\circ}$; (6) scalar data are used for regions poleward of $\pm 60^{\circ}$ or if attitude data were not available; (7) non-polar CHAMP data are only used from local time past midnight. Data sampling interval is 60 s; weights proportional to $\sin \theta$ (where θ is the geographic colatitude) are applied to simulate an equal-area distribution. Anisotropic errors due to attitude uncertainty (Holme & Bloxham 1996; Holme 2000) are considered for all Ørsted vector data and for CHAMP vector data when attitude data from only one star imager are available.

As an example of the data distribution in time, Fig. 1 shows the total number of non-polar magnetic observations for each month. The gaps in the selected CHAMP data about every 130 days is due to the local drift rate of the CHAMP orbit plane and the fact that only CHAMP data past midnight are used. Data from the two other satellites, with their different orbital drift rate, are very useful in filling these gaps. Periods for which less data are available (for instance around 2003) are due to increased geomagnetic activity. Problems with the attitude stability are the reason for the Ørsted data gap around 2007.

To extend the model back in time beyond 1999 February (the launch of the Ørsted satellite), we also use annual differences of observatory monthly means of the north, east and downward components (X, Y, Z) for the years 1997–2006 (annual difference means that the value at time t is obtained by taking the difference between those at $t + 6$ months and $t − 6$ months, thereby eliminating an annual variation in the data). This yields 9860 values of the first time derivative of the vector components, $(dX/dt, dY/dt, dZ/dt)$ for 105 observatories. (Continuous time-series would result in 12 600

values, but data gaps reduce this number to 9860 available values.) These data only contribute to the part of the model that describes the time-changes in the core field. To account for correlated errors due to magnetospheric contributions, we applied the approach of Wardinski & Holme (2006) and weighted the vector components of each observatory according to its 3×3 data covariance matrix (including non-diagonal elements, that is, correlation between the different components). As demonstrated later, adding the observatory data yields a reliable description of the core field changes prior to 1999 (i.e. before satellite data are available) but hardly change the model for the other years, for which the time changes are well resolved by the satellite data.

Parameterization of the CHAOS-2 model follows closely those of CHAOS and xCHAOS (see Olsen *et al.* (2006) for further details). The model consists of two parts: spherical harmonic expansion coefficients describing the magnetic field vector in an 'Earth-Centered Earth-Fixed' (ECEF) coordinate system, and sets of Euler angles needed to rotate the vector readings from the magnetometer frame to the star imager frame. The magnetic field vector in the ECEF frame, $\mathbf{B} = -\nabla V$, is derived from a magnetic scalar potential $V = V^{\mathrm{int}} + V^{\mathrm{ext}}$ consisting of a part, V^{int}, describing internal (core and crustal) sources and a part, V^{ext}, describing external (mainly magnetospheric) sources (including their Earth-induced counterparts). Both are expanded in terms of spherical harmonics.

For the internal part this yields

$$V^{\mathrm{int}} = a \sum_{n=1}^{N_{\mathrm{int}}} \sum_{m=0}^{n} \left(g_n^m \cos m\phi + h_n^m \sin m\phi \right) \left(\frac{a}{r} \right)^{n+1} P_n^m (\cos \theta),$$

$$(1)$$

where $a = 6371.2$ km is a reference radius, (r, θ, ϕ) are geographic coordinates, P_n^m are the associated Schmidt semi-normalized Legendre functions, $\{g_n^m, h_n^m\}$ are the Gauss coefficients describing internal sources and N_{int} is the maximum degree and order of the internal expansion, which is taken here to $N_{\mathrm{int}} = 60$ (for CHAOS and xCHAOS the maximum degree was $N_{\mathrm{int}} = 50$).

The time dependence of the internal Gauss coefficients $\{g_n^m(t), h_n^m(t)\}$ up to $n = 20$ is described by B-splines (Schumaker 1981;
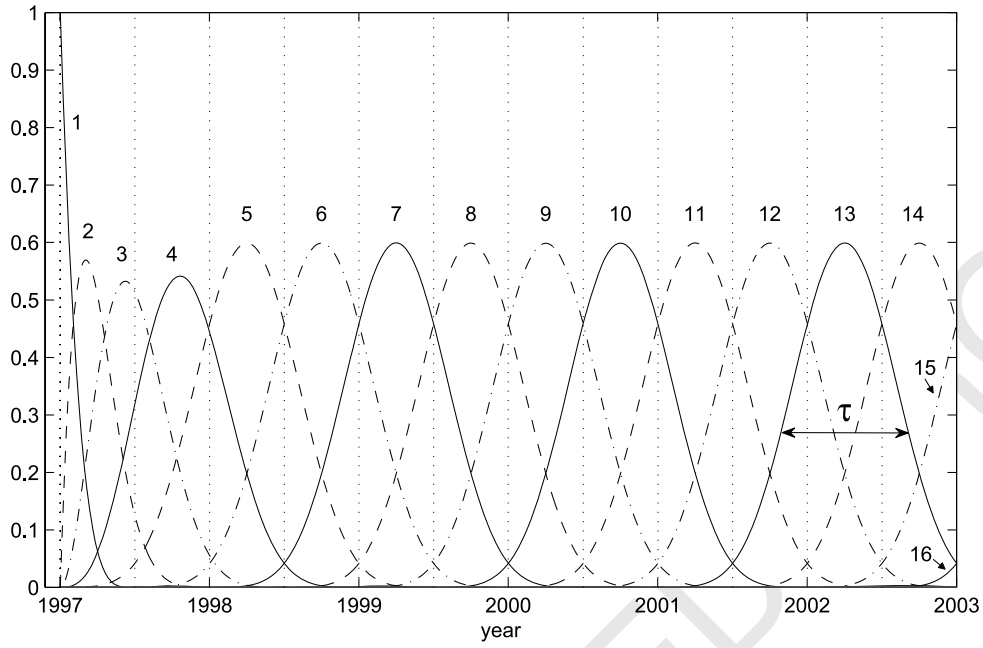
Figure 2. Schematic of the first 6 yr of the 12.5 yr time span covered by the model, showing the first 16 (out of 29 in total) B-spline basic functions, $M_l(t)$, $l = 1$–29, used to represent the time change of each internal Gauss coefficient of degree $n \leq 20$. There are 24 interior knots and 5 exterior knots at each endpoint 1997.0 and 2009.5. See text for definition of the smoothing time τ.

De Boor 2001) in the time interval 1997.0 to 2009.5. However, contrary to the CHAOS model and many other geomagnetic field models which use cubic (i.e. order 4) B-splines (Bloxham 1985; Jackson *et al.* 2000; Wardinski & Holme 2006; Olsen *et al.* 2006), we prefer to use order 5 B-splines, similar to the models CM4 (Sabaka *et al.* 2004) and GRIMM (Lesur *et al.* 2008). Splines of order 4 result in a piecewise linear representation of $\ddot{\mathbf{B}}$, which is not favourable for studying rapid core field changes and geomagnetic jerks. Order 5 splines result in a more smooth representation of $\ddot{\mathbf{B}}$ and are therefore preferable. In order to be able to describe rapid field temporal variations of the core field, we use a 6-month knot separation and four-fold knots at the endpoints, $t = 1997.0$ and 2009.5. This yields 24 interior knots (at 1997.5, 1998.0, ..., 2009.0) and 5 exterior knots at each endpoint, 1997 and 2009.5, resulting in 29 basic B-spline functions, $M_l(t)$. The first 6 yr of the total 12.5 yr time span covered by the model contain 16 of these basis functions and are shown in Fig. 2; the second half (2003.0–2009.5) is symmetric with respect to $t = 2003.25$. Time-dependent terms (for degrees $n = 1$–20) and static terms (for $n = 21$–60) together results in a total of 16 040 internal Gauss coefficients.

We define as a typical resolution or smoothing time τ the 'width' where the spline function drops to half of its maximum value. For the given parametrization (order 5 splines with 6-month knot separation) this results in $\tau = 6.9$ months for $l = 5$–25 as shown in Fig. 2 for the spline function $M_{13}(t)$ (spline functions for $l = 1$–4 and $l = 26$–29 are influenced by edge effects and have different values of τ). We regard τ as a conservative measure of the time scale of fluctuations that can be described with the chosen spline parameterization; fit of more rapid variations (for instance an impulse function) may yield a narrower central peak but introduces significant 'ringing'. In Section 3, we use this definition of smoothing time τ to investigate the effect of model regularization on the temporal resolution of each Gauss coefficient.

The external potential, V^{ext}, describes large-scale magnetospheric sources and is parametrized similar to the CHAOS model:

$$V^{\text{ext}} = a \sum_{n=1}^{2} \sum_{m=0}^{n} (q_n^m \cos mT_d + s_n^m \sin mT_d) \left(\frac{r}{a}\right)^n P_n^m(\cos \theta_d)$$

$$V^{\text{ext}} = a \sum_{n=1}^{2} \sum_{m=0}^{n} (q_n^m \cos mT_d + s_n^m \sin mT_d) P_n^m(\cos \theta_d)$$

$$+ a \sum_{m=0}^{1} (\hat{q}_1^m \cos T_d + \hat{s}_1^m \sin T_d)$$

$$\times \left\{ E_{\text{st}}(t) \left(\frac{r}{a}\right) + I_{\text{st}}(t) \left(\frac{a}{r}\right)^2 \right\} P_1^m(\cos \theta_d)$$

$$+ a \sum_{n=1}^{2} q_n^{0,\text{GSM}} R_n^0(r, \theta, \phi), \tag{2}$$

where θ_d and T_d are dipole colatitude and dipole local time, respectively, and E_{st}, I_{st} are time-series of the decomposition of the D_{st}-index, $D_{\text{st}}(t) = E_{\text{st}}(t) + I_{\text{st}}(t)$, into external and induced parts, respectively (Maus & Weidelt 2004; Olsen *et al.* 2005).

The first two lines of this equation represent an expansion in the 'Solar Magnetic' (SM) coordinate system and describe mainly contributions from the magnetospheric ring current. The expansion in 'Geocentric Solar Magnetospheric' (GSM) coordinates used in the last term describes contributions from magnetotail and magnetopause currents. The functions R_n^0 are modifications of the Legendre functions to account explicitly for induced field contributions due to the wobble of the GSM z-axis with respect to the Earth's rotation axis (see Olsen *et al.* 2006, for details).

Large-scale magnetospheric fields that are not described by $E_{\text{st}}(t)$, $I_{\text{st}}(t)$ are accounted for by the first line of the equation: we solve for time-varying degree-1 coefficients in bins of 12 hours length (for $n = 1$, $m = 0$), resp. 5 d length (for $n = m = 1$), similar as for the CHAOS model (see Olsen *et al.* 2006, for details). We also worked with much longer bins but found that this results in increased power of the high-degree secular variation coefficients; the chosen small bin size thus helps to improve the determination of the high-degree secular variation.

In total this results in 5825 coefficients describing the external field.

Finally, and again following the CHAOS model parameterization, we perform an in-flight instrument calibration and solve for the Euler angles of the rotation between the coordinate systems of the vector magnetometer and of the star sensor that provide attitude information. For the Ørsted data, this yields two sets of Euler angles, while for CHAMP we solve for Euler angles in bins of 10 d (resulting in 195 sets of angles), to account for the thermomechanical instabilities of the magnetometer/star-sensor system. This yields additional $3 \times (2 + 195) = 591$ model parameters. The total number of model parameters is $16\,040 + 5825 + 591 = 22\,456$.

These model parameters are estimated by means of a regularized 'Iteratively Reweighted Least-Squares' approach using Huber weights, minimizing the cost function

$$\mathbf{e}^T \underline{\underline{C}}^{-1} \mathbf{e} + \lambda \mathbf{m}^T \underline{\underline{\Lambda}} \mathbf{m}, \tag{3}$$

where $\mathbf{m}$ is the model vector and the residuals vector $\mathbf{e} = \mathbf{d}_{obs} - \mathbf{d}_{mod}$ is the difference between observation $\mathbf{d}_{obs}$ and model prediction $\mathbf{d}_{mod}$. The data covariance matrix $\underline{\underline{C}}$ contains the data errors multiplied by Huber weights (to account for the non-Gaussian distribution of the data residuals); its non-diagonal elements accounts for the anisotropic errors due to attitude noise. Details on the construction of the data covariance matrix and the choice of the *a priori* data errors can be found in section 3.1 of Olsen (2002). $\underline{\underline{\Lambda}}$ is a block diagonal regularization matrix which constrains the second and higher order time derivatives of the core field. Only elements corresponding to the spline coefficients are non-zero; they are given by

$$\frac{(n+1)}{\Delta t} \left(\frac{a}{c}\right)^{2n+4} \int_{t=1997}^{2009.5} \frac{d^2 M_l(t)}{dt^2} \frac{d^2 M_k(t)}{dt^2} \, dt, \tag{4}$$

with $\Delta t = 2009.5 - 1997 = 12.5$ yr, which minimizes the mean squared magnitude of $|\ddot{\mathbf{B}}|$, integrated over the core surface $d\Omega$ (radius $c = 3485$ km) and averaged over time:

$$\langle |\ddot{\mathbf{B}}|^2 \rangle = \frac{1}{\Delta t} \int_{t=1997}^{2009.5} \int \left| \frac{\partial^2 \mathbf{B}}{\partial t^2} \right|^2 \, d\Omega \, dt = \mathbf{m}^T \underline{\underline{\Lambda}} \mathbf{m}. \tag{5}$$

This damping is different from that used for CHAOS (for which $|\ddot{\mathbf{B}}|^2$ is minimized at Earth's surface) and xCHAOS (for which

the squared second time derivative of the scalar potential V is minimized at the core surface) and was chosen in order to make our approach similar to previous work (e.g. Shure *et al.* 1982). The parameter λ controls the strength of this regularization, with $\lambda = 0$ corresponding to an undamped model. We derived two models: a smoother (more damped) model, called CHAOS-2s [$\lambda = 3$ $(nT\,yr^{-2})^{-2}$], and a rougher (less damped) one, called CHAOS-2r [$\lambda = 3 \times 10^{-2}$ $(nT\,yr^{-2})^{-2}$]. Note that this regularization directly neither affects the static field nor the first time derivative, which are left undamped.

3 RESULTS AND DISCUSSION

Number of data points, residual means and root mean squared (rms) values of the two model versions are listed in Table 1. Means and rms are weighted values calculated from the model residuals $e = d_{obs} - d_{mod}$ using the Huber weights w found in the last iteration according to

$$\text{mean} = \frac{\sum_i w_i e_i}{\sum_i w_i} \tag{6}$$

$$\text{rms} = \sqrt{\frac{\sum_i w_i e_i^2}{\sum_i w_i}}, \tag{7}$$

where the summations are taken over all data points.

Statistics for the satellite vector data is given in a coordinate system that is defined by the bore-sight of the star imager and the ambient field direction (*cf.* Olsen *et al.* 2000b, for details). Both components $B_\perp$ and B_3 are perpendicular to the main field, while B_B is in its direction.

The CHAOS-2 statistics are similar to those of the CHAOS model (*cf*. table 1 of Olsen *et al.* 2006) with an overall scalar misfit at non-polar latitudes of less than 3 nT rms. The reason for the non-zero mean of the observatory dX/dt (also seen in dZ/dt, although smaller) is unclear.

3.1.1 Spatial spectra

As mentioned before, one goal of CHAOS-2 is to provide a good description of the spatial and temporal structure of the secular

Table 1. Number N of data points, mean and rms misfit (in nT for the satellite data, and in nT yr^{-1} for the observatory data) of the two model versions.

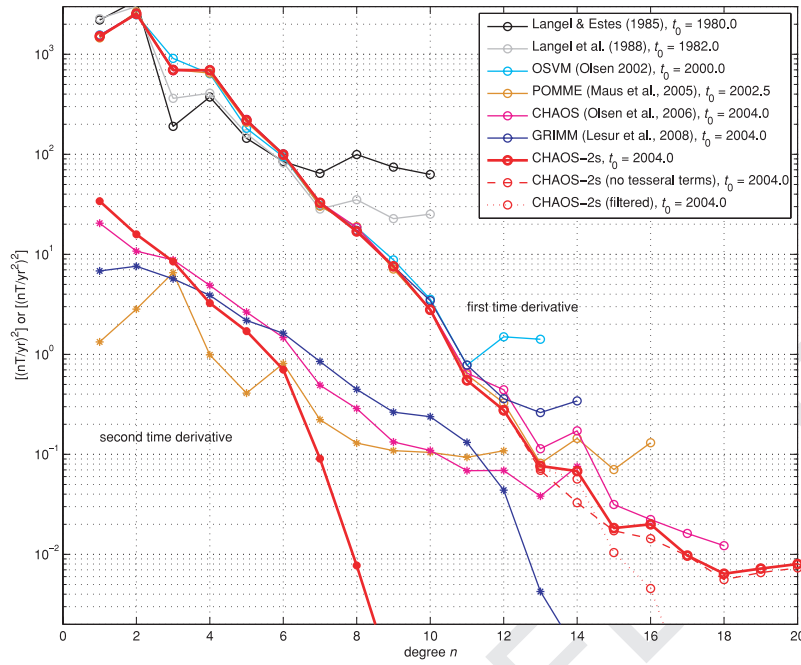|		Component	N	CHAOS-2s Mean	CHAOS-2s rms	CHAOS-2r Mean	CHAOS-2r rms
Satellite	All	F_{polar}	274 564	−0.04	5.54	−0.02	5.50
		$F_{nonpolar} + B_B$	794 522	0.04	2.56	0.03	2.49
	Ørsted	F_{polar}	107 891	0.87	4.40	0.85	4.34
		$F_{nonpolar} + B_B$	399 936	0.34	2.50	0.34	2.43
		$B_\perp$	144 592	−0.02	7.73	−0.02	7.71
		B_3	144 592	−0.01	3.63	0.00	3.59
	CHAMP	F_{polar}	131 344	−0.91	6.74	−0.87	6.71
		$F_{nonpolar} + B_B$	251 046	−0.52	2.60	−0.51	2.53
		$B_\perp$	236 848	0.06	3.70	0.07	3.65
		B_3	218 860	−0.01	3.71	−0.02	3.63
	SAC-C	F_{polar}	35 329	−0.02	4.25	0.00	4.19
		$F_{nonpolar}$	143 540	0.16	2.63	0.14	2.58
Observatory		dX/dt	9860	−2.74	13.42	−2.50	13.38
		dY/dt	9860	0.17	11.41	0.07	11.27
		dZ/dt	9860	0.92	9.91	0.86	9.61

Figure 3. Mauersberger–Lowes spectra of first and second time derivatives at Earth's surface and model epoch t_0 for various magnetic field models.

variation. To assess the quality of the spatial description it is helpful to look at the Mauersberger–Lowes spectra at a given epoch. The static field and first time derivative coefficients of the two model versions CHAOS-2s and CHAOS-2r are very similar (although of course not identical), especially for degrees $n > 10$. Let us in following concentrate on the smoother model CHAOS-2s. Fig. 3 shows spectra of the first and second time derivatives of various models and is an update of fig. 2 of Olsen *et al.* (2006). It demonstrates the improvement in determining secular variation over the last decades, from models derived using Magsat satellite data (Langel & Estes 1985; Langel *et al.* 1988), to models derived from data taken during the first years of the 'International Decade' (Olsen 2002; Maus *et al.* 2005) and to the very recent models CHAOS (Olsen *et al.* 2006), GRIMM (Lesur *et al.* 2008) and CHAOS-2 (this paper). The spectrum of the xCHAOS model (Olsen & Mandea 2008) is not shown as it is almost identical to that of CHAOS-2. The spectrum of the first time derivative of the latter decreases down to a level of less than 10^{-2} [nT (yr)$^{-1}$]^2 for spherical harmonic degrees above $n = 16$. This suggests that core field time changes (averaged over several years, *cf.* the discussion on temporal resolution below) down to spatial scales corresponding to spherical harmonic degree $n = 15$ or 16 are robustly described by CHAOS-2.

When looking at the secular variation spectrum in more detail, the increased power at the even spherical harmonic degrees $n = 16$ and 14, and to some extend also 12, is striking. Most of the power at degree $n = 14$ is in the tesseral coefficients ($\dot{g}_{14}^{14} = -0.043$ nT yr^{-1} is by far the largest coefficient of degree $n = 14$, followed by $\dot{h}_{14}^{14} = -0.022$ nT yr^{-1}), and setting the tesseral coefficients for $n > 10$ to zero results in a spectrum shown by the dashed curve. It is still unclear whether the increased power of the tesseral coefficients for $n = 14$ and 16 is only by chance, caused by the given data distribution, or whether it reflects a small-scale low-latitude feature in the secular variation. Finlay & Jackson (2003) found evidence for equatorially dominated magnetic field changes in historic magnetic field data described by the gufm1 model of Jackson *et al.* (2000); however, their model is spatially regularized and describes only

structures corresponding to spherical harmonic degrees $n \leq 10$ or so.

Also shown in Fig. 3 are spectra of the second time derivative (secular acceleration) for some models. Note that this part of the CHAOS, GRIMM and CHAOS-2 models is damped. Compared to GRIMM, the secular acceleration spectrum of CHAOS-2s has more power at spherical harmonic degrees $n \leq 3$, while that of GRIMM is stronger for $n > 4$. Note, however, that the secular acceleration power heavily depends on the chosen damping parameter λ.

In addition to model version CHAOS-2s we also determined a rougher model version, denoted as CHAOS-2r, by reducing the damping parameter λ. The spectra shown in Fig. 3 are for a certain epoch t_0. A non-zero secular acceleration (second time derivative) results in time changes of the secular variation (first time derivative). Fig. 4 shows these spectra for CHAOS-2s [left-hand side, $\lambda = 3$ (nT yr^{-2})$^{-2}$] and CHAOS-2r [right-hand side, $\lambda = 3 \times 10^{-2}$ (nT yr^{-2})$^{-2}$] and various epochs. The colour of the spectrum indicates the model epoch, varying from blue (for $t_0 = 2000.0$) to red (for $t_0 = 2007.0$). The secular variation spectra of the two model versions are very similar despite of the different secular acceleration spectra (which is due to the different regularization parameter λ chosen for the two model versions). The decrease of secular acceleration power towards the model start (blue curves) is, however, unphysical and probably caused by the lack of satellite data.

3.1.2 Temporal resolution

As shown in Fig. 2, the smoothing time of each spline function (except those near the end points) is $\tau = 6.9$ months. In case of a non-regularized model ($\lambda = 0$), this directly maps into the smoothing time of each Gauss coefficient $g_n^m(t)$, $h_n^m(t)$, $n = 1$–20. However, model regularization results in smoothing times τ that are different for each Gauss coefficient and time dependent (because of the uneven data distribution in time). Let $\underline{\underline{A}}$ be the data kernel matrix that connects the model vector $\mathbf{m}$ with the data vector $\mathbf{d} = \underline{\underline{A}}\mathbf{m}$ (for simplicity we here only consider the case of a linear model). The
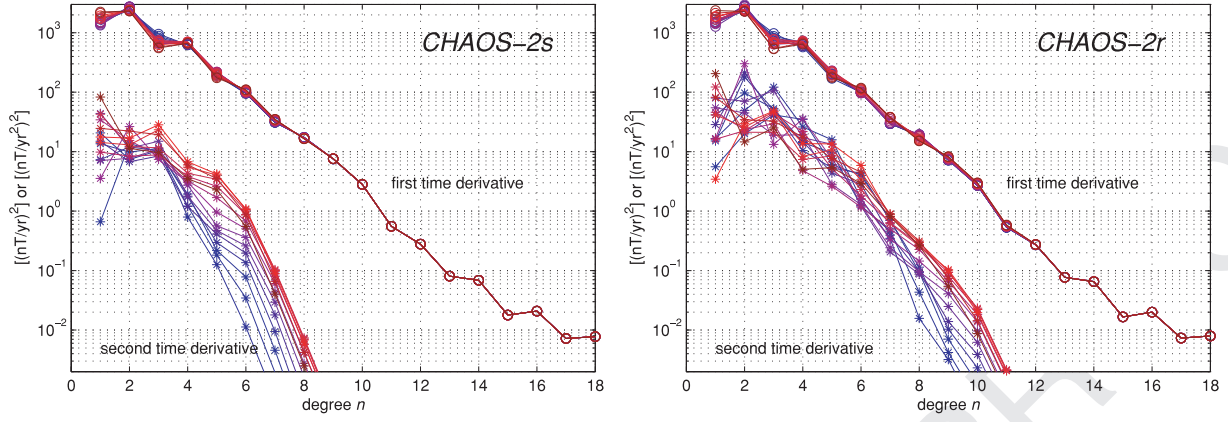
Figure 4. Mauersberger–Lowes spectra of first and second time derivatives at Earth's surface for CHAOS-2s (left-hand side) and CHAOS-2r (right-hand side). The different curves correspond to different epochs t_0 indicated by the colour, from $t_0 = 2000.0$ (blue) in steps of 6 months until $t_0 = 2007.0$ (red).

model resolution matrix is defined as (Menke 1984)

$$\underline{\underline{R}} = (\underline{\underline{A}}^T \underline{\underline{C}}^{-1} \underline{\underline{A}} + \lambda \underline{\underline{\Lambda}})^{-1} (\underline{\underline{A}}^T \underline{\underline{C}}^{-1} \underline{\underline{A}}).$$

For the case of no regularization ($\lambda = 0$) $\underline{\underline{R}} = \underline{\underline{1}}$ is a unit matrix.

Korte & Constable (2008) investigated the temporal resolution of their magnetic field models CALS7xK, the time variation of which is described by splines in a similar way as that chosen here. Following Silverman (1984) and Constable & Parker (1988), they investigate temporal resolution by looking at the local bandwidth of the equivalent kernel. Here, we follow a different path to investigate the temporal resolution of our model. Let us assume that the time dependence of each Gauss coefficient is given by one single spline function, for instance $M_{13}(t)$. The left-hand part of Fig. 5 shows how this input signal $M_{13}(t)$ is modified due to model regularization, that is, $M_{13}(t) \stackrel{R}{\Rightarrow} G_n^m(t)$, for some Gauss coefficients g_n^0 and for the regularization parameters that we have chosen for CHAOS-2s (red) and CHAOS-2r (green), respectively. Similar to our definition of the smoothing time τ for the spline basis function (*cf.* Section 2) we define τ_n^m for the filtered spline functions $G_n^m(t)$ for each Gauss coefficient, as illustrated in Fig. 5 for g_3^0 of model CHAOS-2s. The regularization parameter chosen for CHAOS-2r has almost no influence on the temporal resolution of g_1^0 for that model, which is the reason why $\tau_1^0 \approx \tau_{M_{13}} = 6.9$ months. However, regularization has stronger influence on higher degree terms (as expected), and results in $\tau_3^0 = 7.4$ months and $\tau_5^0 = 9.9$ months. For model

CHAOS-2s the smoothing times are considerable larger: $\tau_1^0 = 8.1$ months, $\tau_3^0 = 14.5$ months, and $\tau_5^0 = 25.6$ months. Terms of even higher degree are so heavily smoothed that it is difficult to determine a meaningful smoothing time (since the filtered spline function does not drop below half of its maximum value in the considered time span); we find that for degrees $n > 7$ the first time derivative (secular variation) of model CHAOS-2s is essentially an average over the whole data period of 12 yr and thus represents a mean rather than an instantaneous linear secular variation. Our analysis confirms that the smoothing time mainly depends on spherical harmonic degree n but is almost independent on the order m, as expected for a regularization that depends only on n but not on m.

While the left-hand part of Fig. 5 shows as an example the smoothing time τ_3^0 around 2003 [i.e. at the maximum of the spline basis function $M_{13}(t)$], its right-hand part shows the time dependence of τ_n^0. The regularization has stronger effect at the beginning because of the less amount of data, which is the reason for the increase of τ_n^0 before 2002.

3.1.3 Fit to observatory monthly means

An assessment of the quality of the temporal description of CHAOS-2 is possible by comparing observed and modelled field variations as monitored by ground observatories. Fig. 6 shows the fit to the first time derivative at the four observatories Niemegk (NGK) in
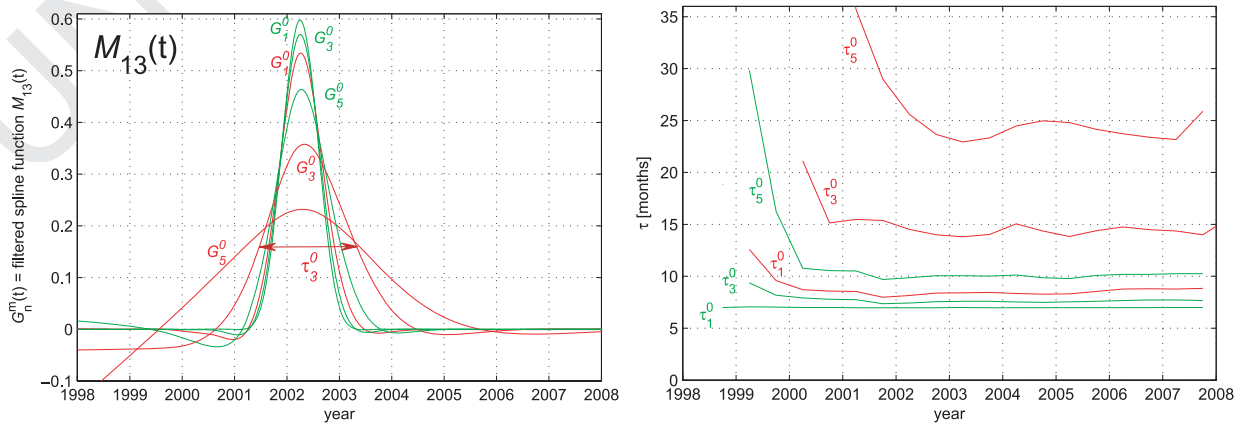
Figure 5. Filtered basis spline function output $G_n^m(t)$ for 2003 (left-hand side) and time dependence of smoothing time τ_n^m (right-hand side) for selected Gauss coefficients and for CHAOS-2s (red) and CHAOS-2r (green).
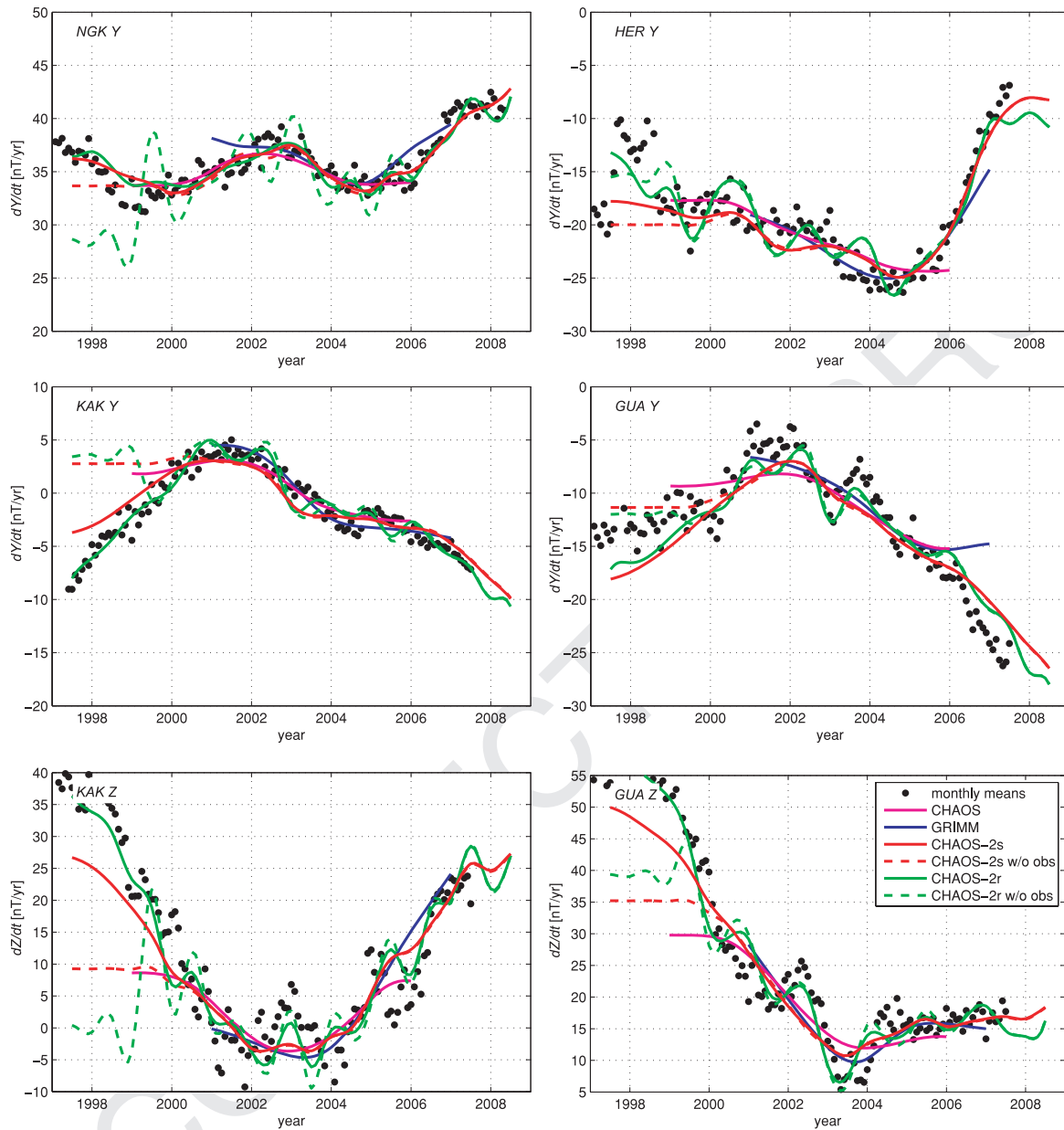
Figure 6. First time derivative of the East component in the geomagnetic frame, dY/dt, resp. of the vertical component, dZ/dt, at the observatories Niemegk (NGK), Hermanus (HER), Kakioka (KAK) and Guam (GUA). Symbols refer to observations (annual difference of monthly means), whereas the solid curves indicate predicted values based on the models CHAOS (magenta), GRIMM (blue), CHAOS-2s (red) and CHAOS-2r (green). Versions of CHAOS-2 obtained without observatory data are shown by the dashed red, resp. green, curves.

Europe, Kakioka (KAK) in Japan, Guam (GUA) in the Pacific, and Hermanus (HER) in South Africa, for some field models. The CHAOS-2s model (red curve) describes rapid time changes much better than the CHAOS model (magenta curve) and about equally well as the xCHAOS model (not shown). Model values of a version of CHAOS-2s obtained without observatory data are shown by the dashed red curve; they differ from CHAOS-2s before 1999 but are very similar for years when satellite data are available.

CHAOS-2s yields a superior description of the observed field variation compared to CHAOS and GRIMM over the entire decade, which is not surprising given the more limited data time span used when deriving the two other models (CHAOS: 1999–2005; GRIMM; 2001–2005). However, there are rapid field variations (for instance in the Z-component of KAK and GUA between 2002 and

2004) that are not described by CHAOS-2s. These changes occur so fast that they can not be described by splines (of order 5 or less) with knot separation of 1 yr or longer, as it is the case for CHAOS and GRIMM. When trying to fit dZ/dt at KAK, resp. GUA, with splines we find that a knot spacing of 8 months or shorter is needed (which is the reason for changing the knot-spacing from 1 yr for CHAOS and xCHAOS to 6 months for CHAOS-2).

Are these rapid field changes of core origin, or are they due to contamination by external (ionospheric and magnetospheric) sources? Fig. 6 shows that CHAOS-2r describes some of the rapid field changes seen in the vertical component at KAK and GUA better than the more heavily regularized version CHAOS-2s. Interestingly, a less regularized model determined from satellite data alone (without observatory data, green dashed curve) describes these rapid field

changes, too. Given the different sampling regions (at the ground, resp. above the ionosphere) and data selection criteria of observatory and satellite data (observatory monthly means are determined by averaging all days and all local times, whereas the satellite data used for CHAOS-2 are only taken from geomagnetically quiet times

and dark conditions), this agreement indicates that these rapid field changes are of internal (core) origin. Further evidence is given by the fact that these fluctuations are describable by an internal potential field (*cf.* the dashed green curve of Fig. 6 which shows a model derived without observatory data), which speaks against a
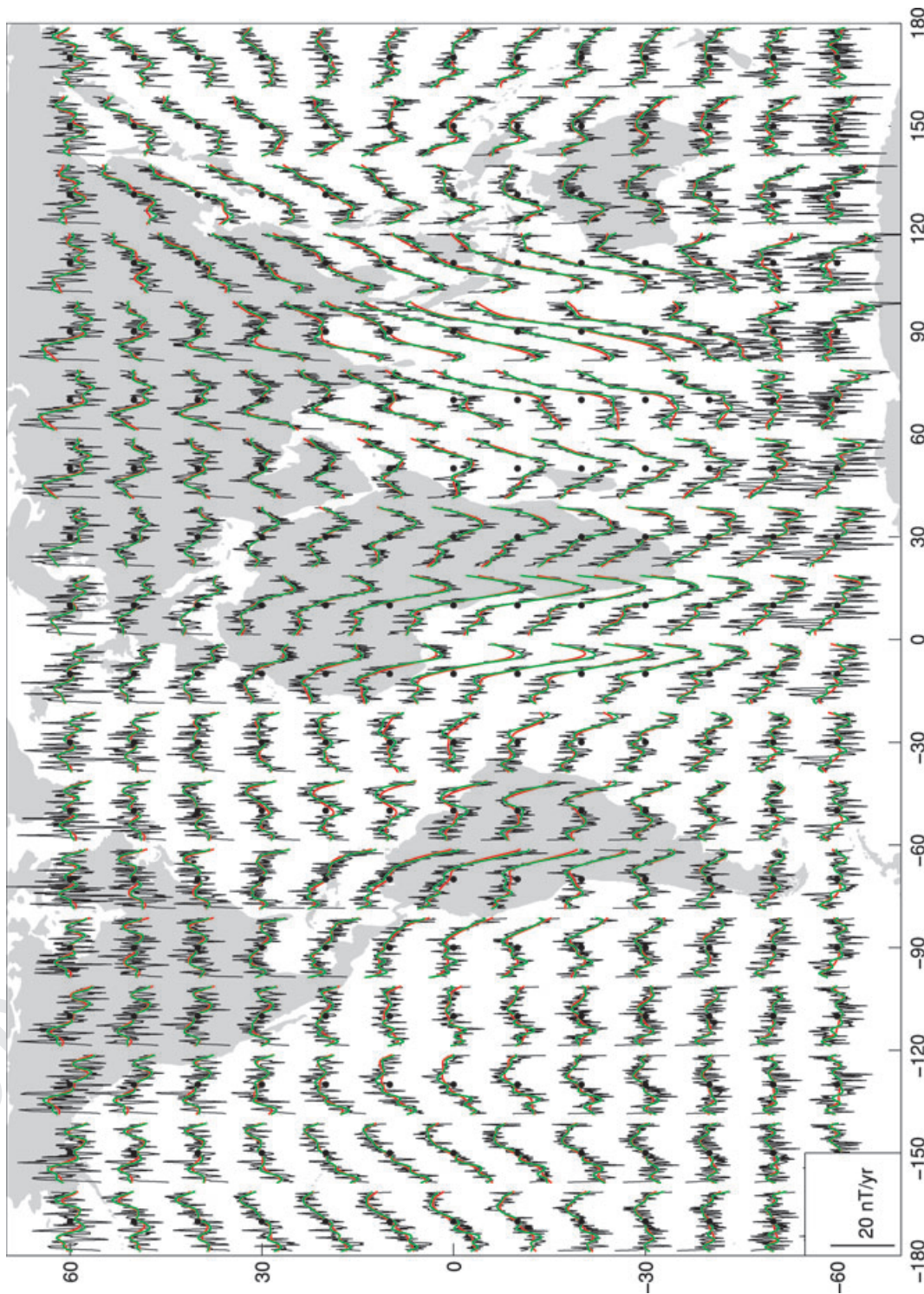

Figure 7. Time-series of dZ/dt (annual differences of monthly means) at 400 km altitude, for the years 2001–2009. Values obtained from CHAMP satellite vector data (after removal of monthly estimates of the external field) are shown in black, predicted values of the CHAOS-2s model in red, and predicted values of the less regularized model CHAOS-2r in green. The left-hand end-point of each curve corresponds to 2001 January, whereas the right-hand end-point corresponds to 2009 March. The mean value was subtracted from each time-series. Locations of the 'virtual observatories' are shown by black dots. Polar regions have been excluded due to their strong contamination by ionospheric current systems.

magnetospheric origin. Finally, also an induced origin can be ruled out since the superposition of external (inducing) and internal (induced) signal is measured and thus the field would no longer be describable by a purely internal field. To investigate further a possible external origin we used the CM4 model (Sabaka *et al.* 2004) and synthesized hourly mean values of the magnetospheric, ionospheric and Earth-induced magnetic field contributions from which we calculated synthetic monthly mean values following usual observatory practice. Comparing the observed monthly means shown in Fig. 6 with these synthetic values (not shown) gives further confidence that the rapid field changes are not of external origin.

To summarize, a definite conclusion on the core origin of the rapid field changes is very difficult, if not impossible. However, the combination of the above listed indications clearly favour a core origin, although each argument alone may only be weakly convincing.

Despite the interesting findings above, we note that reduction of the damping parameter λ results in some field fluctuations that are hardly confirmed by the observatory data (see, for instance, dY/dt at NGK and HER), and it is unlikely that all small 'wiggles' of CHAOS-2r are real. However, the magnitude of these fluctuations are reduced when including observatory data, as expected, which gives us further confident in the quality of CHAOS-2r. To our knowledge CHAOS-2r is the first field model that aims at describing these rapid field changes. Although we believe in the quality of the model at least at non-polar latitudes we recommend extreme caution when interpreting the details of many of the short timescale fluctuations.

Are there other independent data (in addition to the ground observations) that might be used to assess the temporal resolution of the CHAOS-2 model? Following the approach described in Mandea & Olsen (2006) and Olsen & Mandea (2007), we used CHAMP satellite magnetic vector to determine monthly mean values at a regular grid of 'virtual observatories' at 400 km altitude (the mean CHAMP altitude) for the time interval 2001 January–2009 March. Fig. 7 is an extension in time of fig. 7 of Olsen & Mandea (2007) by 2 yr and shows the obtained 'virtual observatory' time-series together with values from CHAOS-2s (red) and CHAOS-2r (green). This data set further demonstrates that CHAOS-2r fits rapid core field changes better than CHAOS-2s, especially at non-polar latitudes. An interesting feature is seen west of Africa, where the foci of rapid secular variation (i.e. a change in slope of the first time derivative, corresponding to a sudden jump in the second time derivative) is seen around 2007. Note that the virtual observatory monthly means are determined from all CHAMP data (regardless of geomagnetic activity and local time), whereas CHAOS-2 uses less than 20 per cent of all available data. We therefore regard those satellite-based monthly means as an independent data set that allows an assessment of the CHAOS-2 model.
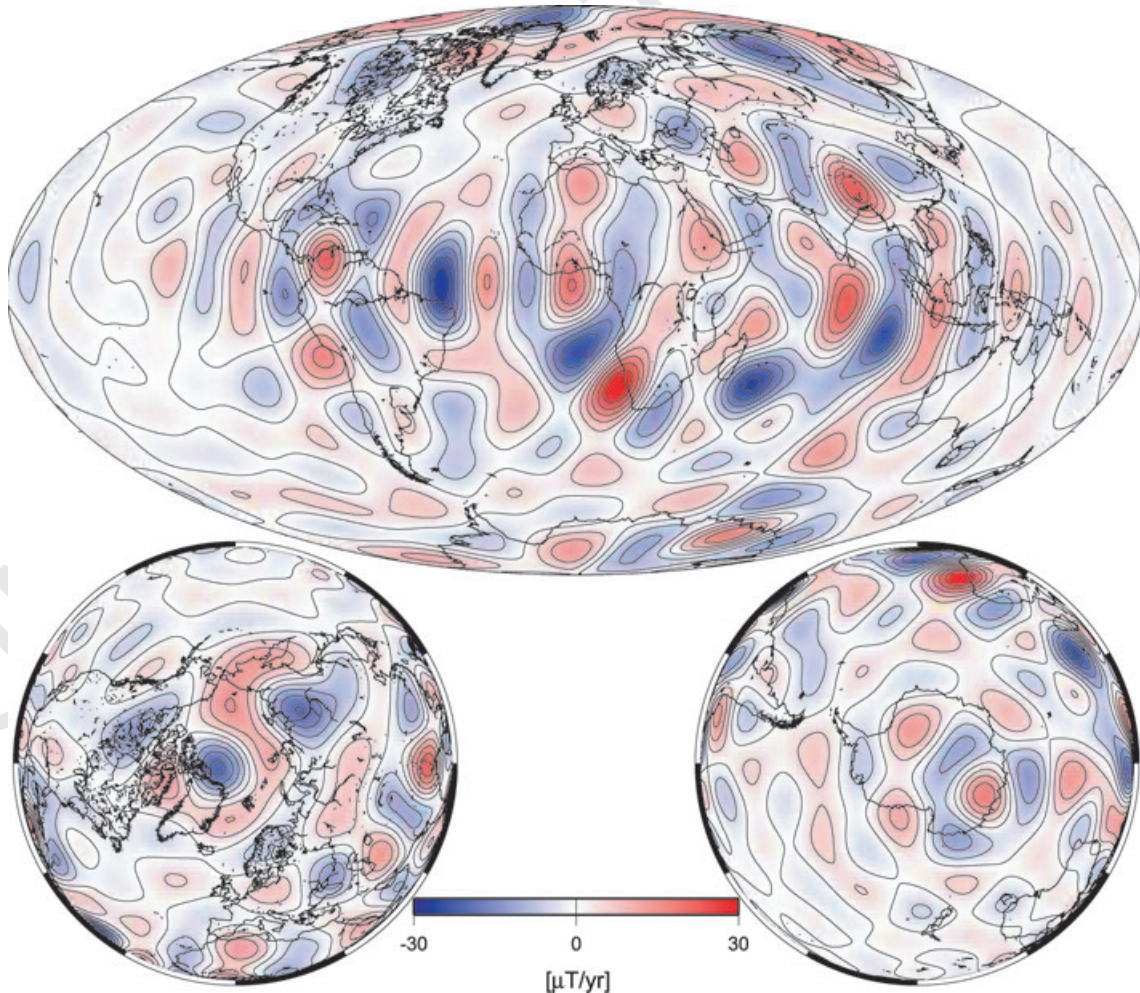
Figure 8. First time derivative, dZ/dt, at the core surface in 2004.0 as given by the CHAOS-2s model. Coefficients of degree larger than 14 are damped. Contour interval is 5 μT yr^{-1}.

A closer investigation of the curves reveals three areas with interesting secular variation. They are roughly delimited by the latitudinal bands $-45°$ to $45°$ and, from West to East, by the longitude $-10°$E to $10°$E, $30°$E to $50°$E, and $70°$E to $90°$E. The central region is characterized by a clear V-shape rapid change in the secular variation around 2005, indicating a jerk. On each side the secular variation is dramatically decreasing (west of $30°$E) or increasing (east of $50°$E). This observation seems to suggest a motion of the foci of rapid secular variation in an east–west direction.

Finally, we show in Fig. 8 a map of dZ/dt at the core–mantle boundary. The secular variation spectrum is almost 'flat' at that depth, which would result in 'ringing' when plotting a truncated spherical harmonic expansion that has not converged. In order to avoid this, we have filtered (damped) the secular variation coefficients according to Wardinski & Holme (2006):

$$\dot{g}^m_{n,\text{filtered}} = \dot{g}^m_n \frac{1}{1 + \mu \left(\frac{a}{c}\right)^{2n+4}} \tag{8}$$

(and similar for $\dot{h}^m_n$) with $\mu = 3.5 \times 10^{-10}$, where $a = 6371.2$ km and $c = 3485$ km are the radii of the Earth's surface and the outer core, respectively. This filter changes mainly coefficients above $n = 12$ and reduces the amplitude at degree $n = 16$ by a factor of 2 (those of degrees $n = 14$ to 18 are reduced (multiplied) by a factor of 0.92, 0.78, 0.51, 0.23 and 0.09). The spectrum (at Earth's surface) of this spatially filtered model is shown in Fig. 3 by the red dotted curve. dZ/dt at the core surface reveals a lot of details, but surprisingly the region of maximum signal is limited to the South Atlantic and Indian ocean, with maximum strength just west of South Africa. The Pacific hemisphere is characterized by a very weak secular variation and less defined structures. The northern and southern polar regions are also curiously different, with larger scales and amplitudes in the north compared to the south. These differences in the temporal variations of the core field are also observed at the Earth's surface by the different behaviour of the magnetic pole motions (Korte & Mandea 2008).

4 CONCLUSIONS

Using more than 10 yr of continuous satellite data, augmented with monthly means from ground magnetic observatories, we have derived a new model, called CHAOS-2, of the static and time-varying part of Earth's magnetic field. This model describes rapid core field variations occurring over only a few months. We have derived two model versions: CHAOS-2s is more heavily regularized in time and therefore smoother, while CHAOS-2r is less heavily regularized and thus rougher.

Model predecessors and the data sets used to construct these models have been widely used (e.g. Holme & Olsen 2006; Gillet *et al.* 2007; Olsen & Mandea 2007, 2008; Pais & Jault 2008) for instance to interpret rapid field variations by means of core flow. We hope that also the CHAOS-2 model described in this paper, which is significantly improved compared to earlier model versions, will ~~also~~ be of use to the scientific community. Although many of the rapid field changes described by the less regularized model version CHAOS-2r are supported by independent data, we recommend extreme caution when interpreting details of the short timescale variations of that model version, especially at polar latitudes, where we recommend to use the more heavily regularized model version CHAOS-2s. Model coefficients and data sets are available at www.space.dtu.dk/files/magnetic-models/CHAOS-2/.

REFERENCES

Bloxham, J., 1985. Geomagnetic secular variation, *PhD thesis*. Cambridge University.

Constable, C.G. & Parker, R.L., 1988. Smoothing, splines, and smoothing splines- Their application in geomagnetism, *J. Comput. Phys.,* **78,** 493–508.

De Boor, C., 2001. A practical guide to splines, *Appl. Math. Sci.,* **27.** [Q3]

Finlay, C.C. & Jackson, A., 2003. Equatorially dominated magnetic field change at the surface of Earth's core, *Science,* **300**(5628), 2084–2086.

Gillet, N., Jackson, A. & Finlay, C.C., 2007. Maximum entropy regularization of time-dependent geomagnetic field models, *Geophys. J. Int.,* **171**(3), 1005–1016.

Holme, R., 2000. Modelling of attitude error in vector magnetic data: application to Ørsted data, *Earth, Planets Space,* **52,** 1187–1197.

Holme, R. & Bloxham, J., 1996. The treatment of attitude errors in satellite geomagnetic data, *Phys. Earth planet. Inter.,* **98,** 221–233.

Holme, R. & Olsen, N., 2006. Core-surface flow modelling from high resolution secular variation, *Geophys. J. Int.,* pp. 518–528.

Jackson, A., Jonkers, A.R.T. & Walker, M.R., 2000. Four centuries of geomagnetic secular variation from historical records, *Phil. Trans. R. Soc. Lond., A,* **358,** 957–990.

Korte, M. & Constable, C.G., 2008. Spatial and temporal resolution of millennial scale geomagnetic field models, *Adv. Space Res.,* **41**(1), 57–69, doi:10.1016/j.asr.2007.03.094.

Korte, M. & Mandea, M., 2008. Magnetic poles and dipole tilt variation over the past decades to millennia, *Earth, Planets Space,* **60,** 937–948.

Langel, R.A. & Estes, R.H., 1985. The near-Earth magnetic field at 1980 determined from MAGSAT data, *J. geophys. Res.,* **90,** 2495–2509.

Langel, R.A., Ridgway, J.R., Sugiura, M. & Maezawa, K., 1988. The geomagnetic field at 1982 from DE-2 and other magnetic field data, *J. Geomagnet. Geoelectr.,* **40,** 1103–1127.

Langlais, B., Mandea, M. & Ultré-Guérard, P., 2003. High-resolution magnetic field modeling: application to MAGSAT and Ørsted data, *Phys. Earth planet. Inter.,* **135,** 77–91.

Lesur, V., Wardinski, I., Rother, M. & Mandea, M., 2008. GRIMM: the GFZ reference internal magnetic model based on vector satellite and observatory data, *Geophys. J. Int.,* **173,** 382–294.

Mandea, M. & Olsen, N., 2006. A new approach to directly determine the secular variation from magnetic satellite observations, *Geophys. Res. Lett.,* **33,** L15306, doi:10.1029/2006GL026616. [Q4]

Maus, S. & Weidelt, P., 2004. Separating the magnetospheric disturbance magnetic field into external and transient internal contributions using a 1D conductivity model of the Earth, *Geophys. Res. Lett.,* **31,** L12614, doi:10.1029/2004GL020,232.

Maus, S., Lühr, H., Balasis, G., Rother, M. & Mandea, M., 2005. Introducing POMME, the POtsdam Magnetic Model of the Earth, in *Earth Observation with CHAMP, Results from Three Years in Orbit,* eds Reigber, C., Lühr, H., Schwintzer, P. & Wickert, J., pp. 293–298, Springer Verlag, Berlin. [Q5]

Maus, S., Rother, M., Stolle, C., Mai, W., Choi, S., Lühr, H., Cooke, D. & Roth, C., 2006. Third generation of the Potsdam Magnetic Model of the Earth (POMME), *Geochem. Geophys. Geosyst.,* **7,** Q07008. [Q6]

Menke, W., 1984. *Geophysical Data Analysis: Discrete Inverse Theory,* Academic Press, New York.

Olsen, N., 2002. A model of the geomagnetic field and its secular variation for epoch 2000 estimated from Ørsted data, *Geophys. J. Int.,* **149**(2), 454–462.

Olsen, N. & Mandea, M., 2007. Investigation of a secular variation impulse using satellite data: the 2003 geomagnetic jerk, *Earth Planet. Science Lett.,* **255,** 94–105, doi:10.1016/j.epsl.2006.12.008.

Olsen, N. & Mandea, M., 2008. Rapidly changing flows in the Earth's core, *Nat. Geosci.,* **1**(6), 390.

Olsen, N., Sabaka, T.J. & Tøffner-Clausen, L., 2000a. Determination of the IGRF 2000 model, *Earth, Planets Space,* **52,** 1175–1182.

Olsen, N., *et al.*, 2000b. Ørsted initial field model, *Geophys. Res. Lett.,* **27,** 3607–3610.

Olsen, N., Sabaka, T.J. & Lowes, F., 2005. New parameterization of external and induced fields in geomagnetic field modeling, and a candidate model for IGRF 2005, *Earth, Planets Space,* **57,** 1141–1149.

Olsen, N., Lühr, H., Sabaka, T.J., Mandea, M., Rother, M., Tøffner-Clausen, L. & Choi, S., 2006. CHAOS—a model of Earth's magnetic field derived from CHAMP, Ørsted, and SAC-C magnetic satellite data, *Geophys. J. Int.,* **166,** 67–75, doi:10.1111/j.1365-246X.2006.02959.x.

Pais, M.A. & Jault, D., 2008. Quasi-geostrophic flows responsible for the secular variation of the Earth's magnetic field, *Geophys. J. Int.,* **173,** 421–443.

Sabaka, T.J., Olsen, N. & Purucker, M.E., 2004. Extending comprehensive models of the Earth's magnetic field with Ørsted and CHAMP data, *Geophys. J. Int.,* **159,** 521–547, doi: 10.1111/j.1365–246X.2004.02,421.x.

Schumaker, L.L., 1981. *Spline Functions: Basic Theory,* John Wiley & Sons, New York.

Shure, L., Parker, R.L. & Backus, G.E., 1982. Harmonic splines for geomagnetic modelling, *Phys. Earth planet. Inter.,* **28,** 215–229, doi:10.1016/0031-9201(82)90003-6.

Silverman, B.W., 1984. Spline smoothing: the equivalent variable kernel method, *Ann. Stat.,* pp. 898–916.

Thomson, A.W.P. & Lesur, V., 2007. An improved geomagnetic data selection algorithm for global geomagnetic field modelling, *Geophys. J. Int.,* **169**(3), 951–963.

Wardinski, I. & Holme, R., 2006. A time-dependent model of the Earth's magnetic field and its secular variation for the period 1980–2000, *J. geophys. Res.,* **111,** B12101, doi:10.1029/2006JB004401.

Note added in proof: The non-zero mean of the observatory dX/dt and dZ/dt (cf. table 1) are probably caused by external field contributions. We found that the use of 'revised observatory monthly means' which have been corrected for ionospheric and magnetospheric field contributions leads to model mean values that are much closer to zero. A detailed discussion will be the subject of a furthcoming publication.

Q u e r i e s

Dear Author

During the copy-editing of your paper, the following queries arose. Please respond to these by marking up your proofs with the necessary changes/additions. Please write your answers on the query sheet if there is insufficient space on the page proofs. Please write clearly and follow the conventions shown on the corrections sheet. If returning the proof by fax do not write too close to the paper's edge. Please remember that illegible mark-ups may delay publication.

Query Reference	Query	Remarks
Q1	Author: Please check and confirm that you are happy with the section to which this paper has been assigned: a list of all the sections can be found in the Author Guidelines (http://www.wiley.com/bw/ submit.asp?ref=0956-540X & site=1).	Section "Geomagnetism, ..." is ok
Q2	Author: As per journal style only keywords from the keyword list are allowed. No other keywords are allowed, so we have deleted the keywords. Please choose up to six key words from the attached list.	Done.
Q3	Author: Please provide page range or doi code for reference De Boor (2001).	This is a book (part of a series)
Q4	Author: Please check page number.	Citation correct according to publisher: see http://www.agu.org/pubs/crossref/2006/2006GL026616.shtml
Q5	Author: Please check page number.	Citation correct according to publisher: see http://www.agu.org/pubs/crossref/2004/2004GL020232.shtml
Q6	Author: Please provide page range or doi code for reference Maus *et al.* (2006).	Done.
Q7	Author: If reference Olsen &Mandea (2008) is not a one-page article please supply the first and last pages for this article.	Done.
Q8	Author: List all authors if eight or fewer.	Paper has 26 authors.

Key words

Authors are requested to choose key words from the list below to describe their work. The key words will be printed underneath the summary and are useful for readers and researchers. Key words should be separated by a semi-colon and listed in the order that they appear in this list. An article should contain no more than six key words.

GEOPHYSICAL METHODS
Time series analysis
Image processing
Neural networks, fuzzy logic
Numerical solutions
Fourier analysis
Wavelet transform
Instability analysis
Inverse theory
Numerical approximations
    and analysis
Persistence, memory,
    correlations, clustering
Probabilistic forecasting
Spatial analysis
Downhole methods
Tomography
Interferometry
Thermobarometry
Fractals and multifractals
Non-linear differential equations
Probability distributions
Self-organization

GEODESY and GRAVITY
Satellite geodesy
Reference systems
Sea level change
Space geodetic surveys
Seismic cycle
Transient deformation
Gravity anomalies and Earth structure
Geopotential theory
Time variable gravity
Earth rotation variations
Global change from geodesy
Lunar and planetary geodesy and gravity
Radar interferometry
Plate motions
Tides and planetary waves
Acoustic-gravity waves

GEOMAGNETISM and
ELECTROMAGNETISM
Electrical properties
Electromagnetic theory
Magnetotelluric
Non-linear electromagnetics
Archaeomagnetism
Biogenic magnetic minerals
Dynamo: theories and simulations
Environmental magnetism
Geomagnetic excursions
Geomagnetic induction
Magnetic anomalies: modelling
    and interpretation
Magnetic and electrical properties
Magnetic fabrics and anisotropy
Magnetic mineralogy and petrology
Magnetostratigraphy
Palaeointensity

Palaeomagnetic secular variation
Palaeomagnetism applied to
    tectonics
Palaeomagnetism applied to
    geologic processes
Rapid time variations
Remagnetization
Reversals: process, time scale,
    magnetostratigraphy
Rock and mineral magnetism
Satellite magnetics
Marine magnetics and
    palaeomagnetics
Marine electromagnetics

GENERAL SUBJECTS
Geomorphology
Geomechanics
Glaciology
Hydrogeophysics
Ionosphere/atmosphere interactions
Ionosphere/magnetosphere interactions
Gas and hydrate systems
Ocean drilling
Hydrology
Ultra-high pressure metamorphism
Ultra-high temperature metamorphism
Tsunamis
Thermochronology
Heat flow
Hydrothermal systems
Mantle processes
Core, outer core and inner core

COMPOSITION and PHYSICAL
PROPERTIES
Microstructures
Permeability and porosity
Plasticity, diffusion, and creep
Composition of the core
Composition of the continental crust
Composition of the oceanic crust
Composition of the mantle
Composition of the planets
Creep and deformation
Defects
Elasticity and anelasticity
Equations of state
High-pressure behaviour
Fracture and flow
Friction
Fault zone rheology
Phase transitions

SEISMOLOGY
Controlled source seismology
Earthquake dynamics
Earthquake ground motions
Earthquake source observations
Seismic monitoring and test-ban
    treaty verification

Palaeoseismology
Earthquake interaction, forecasting,
    and prediction
Seismicity and tectonics
Body waves
Surface waves and free oscillations
Interface waves
Guided waves
Coda waves
Seismic anisotropy
Seismic attenuation
Site effects
Seismic tomography
Volcano seismology
Computational seismology
Theoretical seismology
Statistical seismology
Wave scattering and diffraction
Wave propagation
Acoustic properties
Early warning
Rheology and friction of
    fault zones

TECTONOPHYSICS
Planetary tectonics
Mid-ocean ridge processes
Transform faults
Subduction zone processes
Intra-plate processes
Volcanic arc processes
Back-arc basin processes
Cratons
Continental margins: convergent
Continental margins: divergent
Continental margins: transform
Continental neotectonics
Continental tectonics: compressional
Continental tectonics: extensional
Continental tectonics: strike-slip
    and transform
Sedimentary basin processes
Oceanic hotspots and
    intraplate volcanism
Oceanic plateaus and
    microcontinents
Oceanic transform and fracture
    zone processes
Submarine landslides
Submarine tectonics and volcanism
Tectonics and landscape evolution
Tectonics and climatic interactions
Dynamics and mechanics of faulting
Dynamics of lithosphere and mantle
Dynamics: convection currents, and
    mantle plumes
Dynamics: gravity and tectonics
Dynamics: seismotectonics
Heat generation and transport
Impact phenomena
Hotspots

Large igneous provinces
Lithospheric flexure
Obduction tectonics
Neotectonics
Diapir and diapirism
Folds and folding
Fractures and faults
Kinematics of crustal and mantle
     deformation
High strain deformation zones
Crustal structure
Mechanics, theory, and modelling
Rheology: crust and lithosphere
Rheology: mantle

PLANETS
Planetary interiors
Planetary volcanism

VOLCANOLOGY
Physics of magma and
     magma bodies
Magma chamber processes
Magma genesis and partial melting
Pluton emplacement
Effusive volcanism
Mud volcanism
Subaqueous volcanism
Explosive volcanism
Volcaniclastic deposits
Volcano/climate interactions
Atmospheric effects (volcano)
Volcanic gases
Lava rheology and morphology
Magma migration and fragmentation
Eruption mechanisms and
     flow emplacement
Physics and chemistry of magma bodies

Calderas
Experimental volcanism
Tephrochronology
Remote sensing of volcanoes
Volcano monitoring
Volcanic hazards and risks

GEOGRAPHIC LOCATION
Africa
Antarctica
Arctic region
Asia
Atlantic Ocean
Australia
Europe
Indian Ocean
North America
Pacific Ocean
South America

MARKED PROOF

Please correct and return this set

Please use the proof correction marks shown below for all alterations and corrections. If you wish to return your proof by fax you should ensure that all amendments are written clearly in dark ink and are made well within the page margins.

Instruction to printer	Textual mark	Marginal mark
Leave unchanged	··· under matter to remain	Ⓙ
Insert in text the matter indicated in the margin	⋏	New matter followed by ⋏ or ⋏②
Delete	/ through single character, rule or underline or ⊢——⊣ through all characters to be deleted	⌀ or ⌀②
Substitute character or substitute part of one or more word(s)	/ through letter or ⊢——⊣ through characters	new character / or new characters /
Change to italics	— under matter to be changed	⌣
Change to capitals	≡ under matter to be changed	≡
Change to small capitals	= under matter to be changed	=
Change to bold type	∿ under matter to be changed	∿
Change to bold italic	≈ under matter to be changed	≋
Change to lower case	Encircle matter to be changed	≢
Change italic to upright type	(As above)	⊥
Change bold to non-bold type	(As above)	⊥
Insert 'superior' character	/ through character or ⋏ where required	� or ⋏ under character e.g. Ỷ or ⋏
Insert 'inferior' character	(As above)	⋏ over character e.g. ⋏
Insert full stop	(As above)	⊙
Insert comma	(As above)	,
Insert single quotation marks	(As above)	Ỷ or ⋏ and/or Ỷ or ⋏
Insert double quotation marks	(As above)	Ỷ or ⋏ and/or Ỷ or ⋏
Insert hyphen	(As above)	⊢⊣
Start new paragraph	⌐	⌐
No new paragraph	⌒	⌒
Transpose	⊔⊓	⊔⊓
Close up	linking ⌒ characters	◯
Insert or substitute space between characters or words	/ through character or ⋏ where required	Y
Reduce space between characters or words	❘ between characters or words affected	↑